University of Dundee

Ultrastructure of COPII vesicle formation in yeast characterized by correlative light and electron microscopy

Melero, Alejandro; Boulanger, Jerome; Kukulski, Wanda; Miller, Elizabeth A

Ultrastructure of COPII vesicle formation in yeast characterized by correlative light and electron microscopy

Alejandro Melero[ID][†],*, Jerome Boulanger, Wanda Kukulski[ID][‡], and Elizabeth A. Miller*
Cell Biology Division, MRC Laboratory of Molecular Biology, Cambridge CB2 0QH, United Kingdom

ABSTRACT Traffic of proteins out of the endoplasmic reticulum (ER) is driven by the COPII coat, a layered protein scaffold that mediates the capture of cargo proteins and the remodeling of the ER membrane into spherical vesicular carriers. Although the components of this machinery have been genetically defined, and the mechanisms of coat assembly extensively explored in vitro, understanding the physical mechanisms of membrane remodeling in cells remains a challenge. Here we use correlative light and electron microscopy (CLEM) to visualize the nanoscale ultrastructure of membrane remodeling at ER exit sites (ERES) in yeast cells. Using various COPII mutants, we have determined the broad contribution that each layer of the coat makes to membrane remodeling. Our data suggest that inner coat components define the radius of curvature, whereas outer coat components facilitate membrane fission. The organization of the coat in conjunction with membrane biophysical properties determines the ultrastructure of vesicles and thus the efficiency of protein transport.

INTRODUCTION

Eukaryotic cells use vesicular membrane carriers to shuttle proteins and lipids between subcellular compartments. These carriers are generated by cytosolic coat proteins capable of concentrating cargo at discrete membrane subdomains and enforcing membrane shape remodeling to generate highly curved vesicles and tubules (Bonifacino and Glick, 2004; Faini *et al.*, 2013). Coat complex protein II (COPII) is responsible for the traffic of proteins from the endoplasmic reticulum (ER) to the Golgi complex, an essential route for one-third of the eukaryotic proteome (Ghaemmaghami *et al.* 2003).

Vesicle formation occurs at ER exit sites (ERES), where the COPII machinery orchestrates cargo selection and membrane bending (Figure 1A; Miller and Barlowe, 2010).

Vesicle formation starts with the small GTPase Sar1, which, upon GTP-binding, inserts an amphipathic α-helix into the cytosolic leaflet of the ER membrane, enabling the recruitment of subsequent coat components, all of which are essential in yeast. The inner coat is composed of the heterodimer Sec23/Sec24, where Sec23 is GTPase activating protein (GAP) for Sar1, and Sec24 is a cargo adaptor that interacts directly with cargo or with cargo receptors through their sorting signals. Together, Sar1(GTP)–Sec23/Sec24 triggers the recruitment of the outer coat, composed of the rodlike heterotetrameric Sec13/Sec31. Assembly of the outer coat into a polyhedral cage is thought to drive membrane deformation into highly curved buds (Stagg *et al.*, 2006), leading to the appearance of a narrow bud neck which undergoes fission, probably facilitated by rounds of GTP hydrolysis on Sar1 (Bi *et al.*, 2007; Hanna *et al.*, 2016; Kurokawa *et al.*, 2016).

Interactions between the outer and inner coat layers drive coat assembly, but also play a regulatory role in coat assembly. An intrinsically disordered region of Sec31 interacts with Sec23 via multiple weak interfaces. One interface accelerates GTP hydrolysis by promoting optimal amino acid positioning within the catalytic pocket (Bi *et al.*, 2007). Additional roles may include coordinating the lateral assembly of the inner coat and stabilizing the coat scaffold (Hutchings *et al.*, 2018; Stancheva *et al.*, 2020). In addition to the
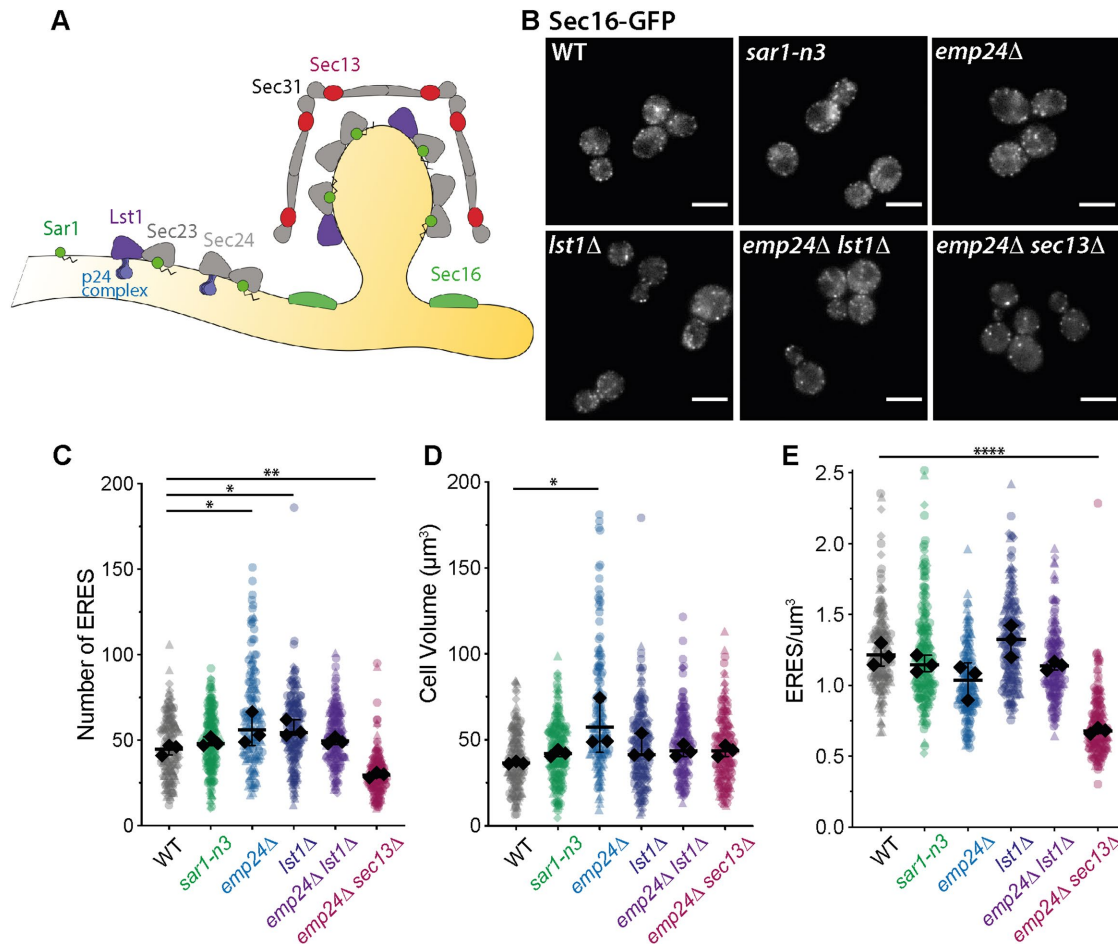
FIGURE 1: (A) COPII assembly scheme. Sar1-GTP binds to the ER surface via an amphipathic helix. Sar1 recruits Sec23/Sec24, with Sec24 binding to cargo and cargo receptors (e.g., p24 complex). Sec23 also forms dimers with Lst1, a paralog of Sec24. Sar1-Sec23/Sec24 recruits Sec13/Sec31, which organizes as a rigid polyhedral structure. Sec16 is a regulatory protein that localizes at ERES and regulates coat polymerization. (B) Visualization of ERES in the indicated yeast strains expressing Sec16-sfGFP. Scale bar is 5 μm. (C–E) Superplots of quantification of ERES abundance and cell volume in COPII-dysfunctional strains, showing total number of ERES per cell, C; cell volume (μm^3; middle panel), D; and ERS abundance per cell volume (ERES/μm^3; right panel), E. Values for individual measurements are represented as dots, with dot shape indicating which of three biological replicas the sample came from. Black dots represent median values for each biological replica; bars indicate the mean and SD between replicas; statistical significance was determined using a one-way ANOVA that compared all five mutant strains with WT (* $p < 0.05$; ** $p = 0.008$; **** $p < 0.0001$).

core COPII coat proteins, various accessory proteins are thought to influence COPII assembly. For example, the essential protein Sec16 also contains intrinsically disordered regions and modulates the GAP activity of the assembled coat by competing with Sec31 for binding to Sec23 (Kung et al., 2011). This activity is thought to stabilize coat assembly and prevent early scission. The dynamics of these various intercoat interactions is thought to contribute the formation of large vesicles in metazoans, including those that traffic large molecules such as procollagen (Raote et al., 2020)

How vesicles of different sizes are generated by the COPII coat remains an important question. Multiple factors likely contribute, including the rate of GTP hydrolysis, which determines coat lifetime on the membrane (Antonny et al., 2001), and organization of the inner coat by accessory proteins (Ma and Goldberg, 2016; Raote et al., 2018). Moreover, distinct properties of the inner coat proteins also seem to influence vesicle size; in yeast, the Sec24 paralog Lst1 increases the average size of COPII vesicles by ~15% (Gomez-Navarro et al., 2020; Miller et al., 2002; Shimoni et al., 2000). The mechanism by which Lst1 drives the formation of larger vesicles re-

mains unknown. Tuning vesicle size to the appropriate cargo burden is not just important in accommodating large cargo proteins (Malhotra et al., 2015). We recently showed that the sorting capacity of COPII vesicles stems at least in part from steric effects: vesicles crowded with cargo proteins preclude the passive leakage of ER resident proteins (Gomez-Navarro et al., 2020). Thus, tuning the ultrastructure of vesicles to accommodate the requisite cargo and maximizing vesicle occupancy are a fundamental aspect of protein quality control.

Despite our knowledge of the parts list of the coat machinery, and a growing understanding of the assembly process, precisely how the COPII coat overcomes the energy barrier to remodel a relatively flat and cargo-crowded membrane into a vesicle with distinct morphology remains unclear. The coat must overcome both the physical opposition conferred by cargo crowding in the lumen and the resistance of the lipid bilayer to changes in shape (Derganc et al., 2013; Stachowiak et al., 2013). In vitro evidence suggests that membrane remodeling can be driven by all components of the coat via different mechanisms (Lee et al., 2005; Zanetti et al., 2013;

Hutchings *et al.*, 2018). However, in vitro techniques fail to recapitulate the complexity of ER architecture and luminal crowding, hence limiting our understanding of the mechanistic requirements of COPII machinery. In cells, vesicle formation at ERES is very dynamic and vesicles are too small to be visualized by light microscopy. Traditional electron microscopy cannot reveal protein localization, and thus offers limited information on the ultrastructure of specific budding events. Here we investigate membrane ultrastructure during COPII vesicle formation using correlative light and electron microscopy (CLEM). We obtained insight into COPII vesicle formation by examining yeast mutants compromised for specific coat subunits and for cargo capture. We find that different COPII coat subunits have specific roles in curvature and force generation, which ultimately determine ultrastructure and thus influence secretion. Our data support a model for COPII vesicle formation where the inner coat components define the radius of curvature, and the outer coat drives membrane remodeling to high curvature and fission.

RESULTS

Inner and outer coat dysfunction modifies the ultrastructure of endoplasmic reticulum exit sites

To understand membrane remodeling at ERES, we used yeast mutants defective in coat assembly, cargo packing, or membrane remodeling (Figure 1A and Supplemental Figure S1). These mutations do not compromise cell viability in vivo, suggesting that cells can adapt to limitations in coat function. To challenge early coat assembly and membrane remodeling, we used a mutant Sar1 strain, *sar1-n3* (Lee *et al.*, 2005). This mutation substitutes two bulky residues for alanine within the N-terminal amphipathic helix, which abolishes the capacity of Sar1 to deform membranes in vitro and reduces export of Glycosylphosphatidylinositol-anchored proteins (GPI-APs) in vivo (Lee *et al.*, 2005). We addressed inner COPII coat function with three different strains: *emp24Δ*, *lst1Δ*, and *emp24Δ lst1Δ*. Emp24 is a member of the p24 family, which forms a cargo–receptor complex required for sorting of GPI-APs into COPII buds (Manzano-Lopez *et al.*, 2015). We used an *emp24Δ* strain to reduce the abundance of bulky cargo at ERES and thus reduce the energy barrier to deformation of the ER membrane (Copic *et al.*, 2012). GPI-APs bound to the p24 complex are preferentially selected for secretion by the cargo adaptor subunit Lst1, a nonessential isoform of Sec24 (D'Arcangelo *et al.*, 2015; Manzano-Lopez *et al.*, 2015). Because Lst1 is associated with large COPII vesicles (Miller *et al.*, 2002; Shimoni *et al.*, 2000), we used the *lst1Δ* background to force the formation of small buds and vesicles. The *emp24Δ lst1Δ* double mutant should yield small vesicles with reduced loads of bulky cargo (Gomez-Navarro *et al.*, 2020). Finally, we assessed the contribution of a rigid outer coat scaffold by analyzing an *emp24Δ sec13Δ* strain, where deletion of Sec13 is tolerated, likely because of reduced GPI-AP traffic, which lowers the energetic cost of bending the ER membrane (Copic *et al.*, 2012).

To visualize ERES, we tagged Sec16 at its chromosomal locus by integrating superfolder GFP (sfGFP) at the C-terminus (Sec16-sf-GFP; Figure 1B). We first asked whether the number and/or distribution of ERES was altered in any of our mutant backgrounds. We acquired image stacks and counted the number of ERES per cell (Figure 1C) and cell volume (Figure 1D) using a custom-made FIJI macro. Only the *emp24Δ sec13Δ* strain showed significant alterations of the number of ERES per cell volume, with an abundance of ERES/μm³ ~40% lower than wild-type (WT; Figure 1E). Having a reduced capacity to deform membranes (*sar1-n3*) or making smaller (*lst1Δ*) and/or less crowded vesicles (*emp24Δ lst1Δ* and *emp24Δ*) did not impact the number or distribution of ERES in yeast cells.

To visualize membrane ultrastructure at ERES, we used correlative light and electron microscopy (CLEM). This method combines the advantages of protein localization by light microscopy with the detailed nanoscale resolution of electron tomography (Kukulski *et al.*, 2011). We have shown recently that CLEM is a suitable tool for analyzing the ultrastructure of COPII vesicles (Gomez-Navarro *et al.*, 2020). Yeast cells were subjected to high-pressure freezing, freeze substitution, and embedding in Lowicryl resin. This approach enables excellent preservation of ultrastructural details, while allowing the use of room-temperature electron microscopy to localize a protein of interest within a tomographic volume (2 × 2 μm by ~300 nm in depth). We acquired fluorescence microscopy images of cells in resin sections and used fluorescent fiducials to obtain a high-precision correlation of ERES marked with Sec16-GFP within electron tomograms (Figure 2A; Supplemental Figure S2). Using this approach, we analyzed the ultrastructure of ERES in WT and mutant cells (Figure 2B; Supplemental Figure S3).

Tomographic reconstructions are detail-rich, enabling us to extract information about the environment surrounding ERES as well as their ultrastructure (Figure 2, C and D). Although this approach does not capture the kinetics of vesicle formation, we can consider the frequency of specific structures as indicative of their lifespan: very transient structures will generally not be well represented in our dataset, whereas longer-lived intermediates will be proportionally more abundant. The majority of WT ERES (~60%) comprise a single bud; occasionally, multiple budding events could be found at the same Sec16-sfGFP correlated region (19%), although we did not observe more than two simultaneous buds per ERES (Figure 2C). Free vesicles fully released from the donor membrane could be observed, with a frequency (0.39 for WT) that we define as the number of vesicles per ERES (i.e., the total number of free vesicles divided by the number of correlated ERES). Sec16-correlated regions occurred with equivalent frequency on ER tubules or cisterna, which were easily designated as ER membranes because of the prevalence of ribosomes on adjacent regions of the continuous donor membrane structure. ERES were often located at regions of existing curvature (fenestrations or membrane junctions), with a minority of ERES found at the nuclear envelope (NE; Figure 2D). We also note the presence of other nearby structures, such as Golgi cisterna, which we defined as flattened cisternal membrane devoid of ribosomes (Supplemental Figure S4).

Comparing the global features of ERES in different mutant backgrounds (Figure 2, C and D), we highlight several significant differences in the frequency of specific budding intermediates. Mutation of the Sar1 N-terminal amphipathic helix (*sar1-n3*) reduced the occurrence of multibudded structures (to 7%) and increased the frequency of free vesicles (~0.8) associated with ERES (Figure 2C). Budding sites in this background were more prevalent on ER tubules (Figure 2D), suggesting that ERES form preferentially on existing areas of curvature when membrane remodeling is compromised (Okamoto *et al.*, 2012).

The *emp24Δ* strain was broadly similar to WT with respect to donor membrane morphology and distribution, whereas the *lst1Δ* strain had reduced occurrence of multibudded structures (Figure 2C). In contrast, the *emp24Δ lst1Δ* double mutant markedly differed from both WT and individual deletions. The frequency of free vesicles (1.22) was three times higher than that of WT, corresponding to an average of more than one free vesicle per ERES, and the predominant budding profile was a flat membrane (Figure 2C). One interpretation of this morphology is that the lifetime of budding intermediates is reduced in the double mutant, with vesicle release occurring more efficiently. Budding sites in the *emp24Δ lst1Δ* double mutant were
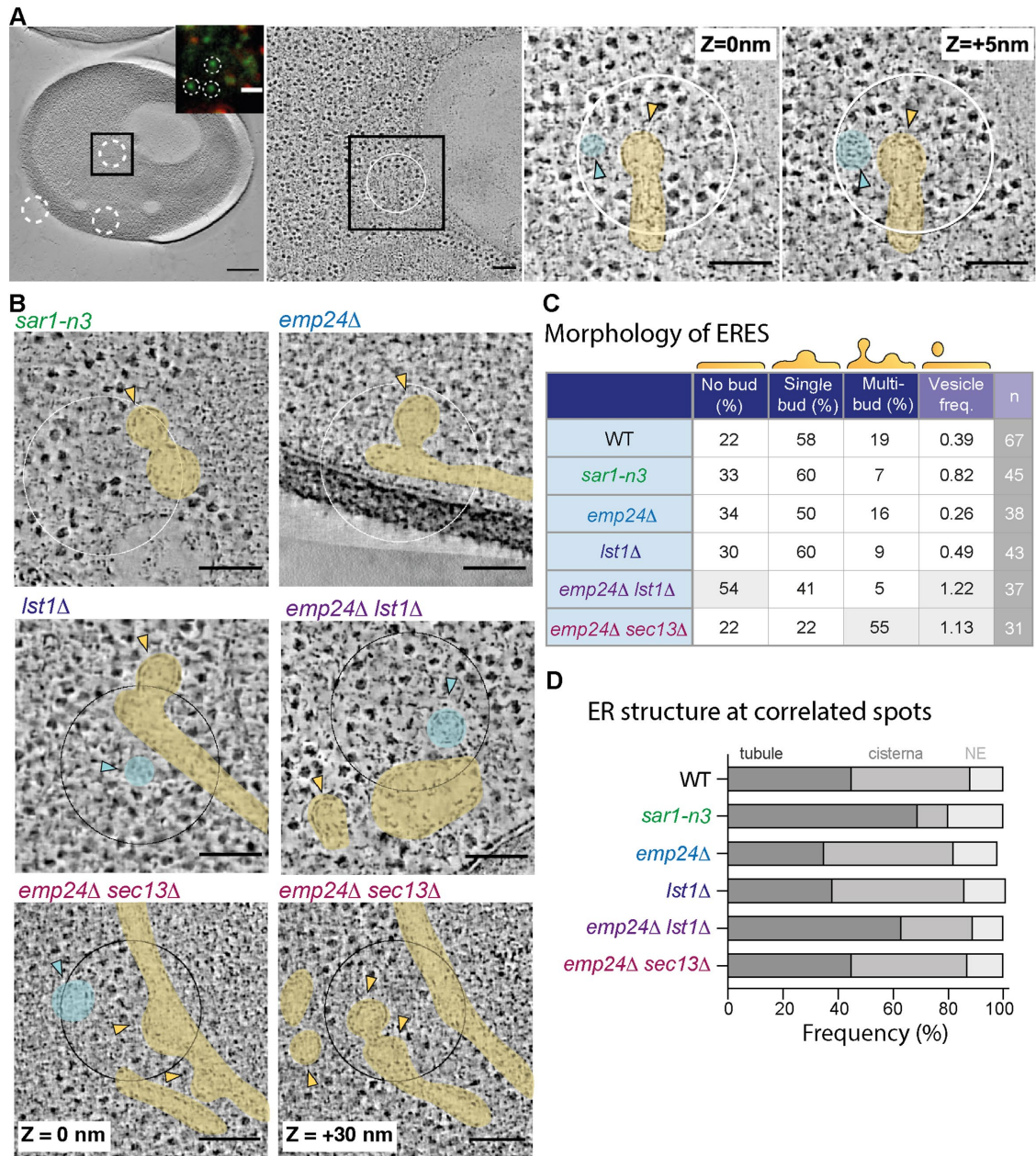
FIGURE 2: (A) CLEM workflow: sections of high-pressure frozen and resin-embedded yeast cells were imaged with fluorescent microscopy (inset, left panel) and scanning transmission electron microscopy (STEM). Fluorescent images were correlated with low-magnification EM images (left panel) using fluorescent fiducials (red spots in inset), enabling the precise localization of Sec16-sGFP positive ERES (green spots in inset; white circles in EM images) within high-magnification tomographic volumes (right panels). Vesicle formation from ER structures (yellow arrow) and free vesicles (cyan arrow) can be found at sites of Sec16-sfGFP signal. Scale bars represent 500 nm in left panel (1 μm in inset) and 100 nm in subsequent panels. (B) Examples of correlated Sec16-sfGFP ERES in COPII dysfunctional strains. For *emp24Δ sec13Δ*, we show two virtual slices of the same tomogram. Scale bars represent 100 nm. (C) Table of ERES ultrastructure categories as percentages of number of correlated Sec16-sfGFP (*n*) subcellular regions; vesicle frequency represents the average number of free vesicles per ERES, quantified as the total number of free vesicles divided by the total number of ERES. Gray shaded sections represent major differences from WT. (D) Bar plot representing the frequency (%) of Sec16-correlated spots in different ER subregions. In the absence of visible buds, the nearest ER membrane to the centroid of the Sec16-sfGFP signal was considered as the corresponding ER subregion. NE stands for nuclear envelope.

more frequently found on tubular ER (Figure 2D). Finally, the budding profile of the *emp24Δ sec13Δ* strain, with a compromised outer coat, was shifted toward bud production, with 55% of ERES occurring as multiple buds (Figure 2C). In some cells, these structures formed a complex network of tubules decorated with buds and pearled tubes (Supplemental Figure S5). ERES in *emp24Δ sec13Δ* cells were also associated with significantly more free vesicles per ERES (vesicle frequency of 1.13, corresponding to an average of one vesicle per ERES). Our CLEM tomography analysis of ERES thus revealed that the ultrastructure of vesicle biogenesis adapts to the physical features
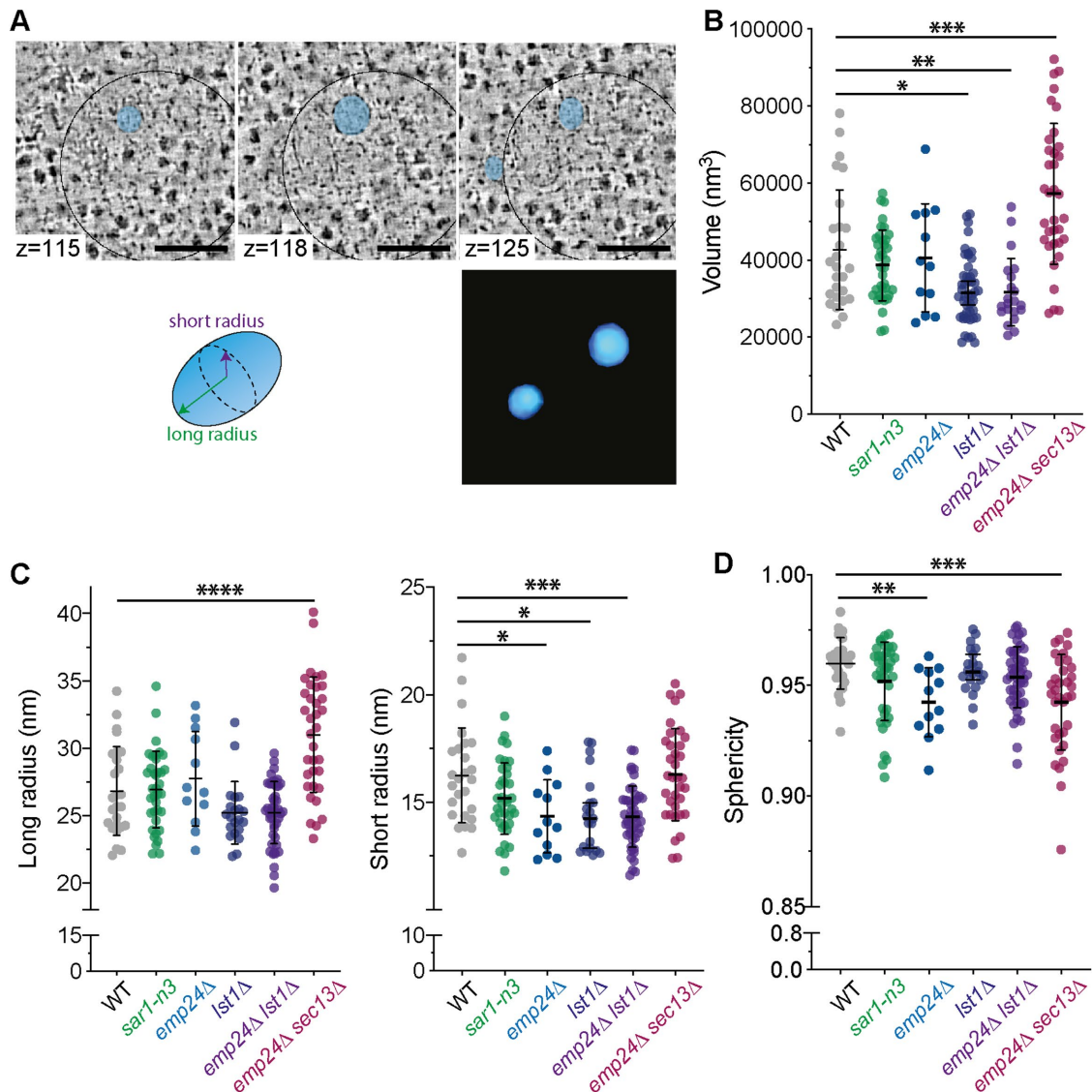
FIGURE 3: (A) Upper panels: Sequential virtual slices of a Sec16-sfGFP correlated site showing two free COPII vesicles (false colored in cyan) next to a budding site. Scale bars are 100 nm. Lower left: Diagram defining axes of ellipsoidal vesicles. The centroid of the vesicle was used to calculate the longest radius (farthest point to the centroid) and the shortest radius (nearest point to the centroid). Lower right: Segmented volume of upper panel vesicles. (B) Plot of the volume (nm^3) of free COPII vesicles in the strains indicated. Each point corresponds to a vesicle measured in the indicated strain. Bars represent median value and 95% confidence interval. (C) Analysis of the two major axes of free COPII vesicles. Using the segmented volumes of COPII vesicles, we determined the longest and shortest radius from the centroid for each vesicle in WT and COPII-dysfunctional strains. Each point corresponds to a vesicle in the indicated strain. Bars represent median with 95% confidence interval. (D) Plot of the sphericity of vesicles, where 1 equals a perfect sphere and <1 indicates ellipsoidal morphologies. Statistical tests were one-way ANOVA with Tukey's correction for multiple comparisons, where all five mutant strains were compared with WT (* $p < 0.05$; ** $p < 0.01$; ** $p < 0.001$; **** $p < 0.0001$).

of the coat and the cargo load. Altering inner coat function (*sar1-n3* and *emp24Δ lst1Δ*) increased the frequency of free vesicles, perhaps reflecting more efficient vesicle release. In contrast, reducing the rigidity of the outer coat seems to prolong bud formation, resulting in extended multibudded structures.

Ultrastructural changes in COPII vesicles suggest distinct roles in membrane remodeling and scission for inner and outer coat layers

We next sought to quantify vesicle morphology by obtaining quantitative morphological descriptors. We first used a semiautomated

segmentation method to segment the membrane boundaries of free vesicles in tomographic reconstructions (Figure 3A; Machado *et al.*, 2019)). Using the segmented surface mesh, we calculated the volume of the vesicle (Figure 3B), determined its centroid, and measured the longest and shortest distances from the centroid to the vesicle surface, equivalent to the major and minor radii of the vesicle (Figure 3A). As reported previously (Gomez-Navarro *et al.*, 2020), vesicle volume was reduced in *emp24Δ lst1Δ* mutants and increased in *emp24Δ sec13Δ* double mutants (Figure 3B). As expected, we saw similar reduction in vesicle volume in the *lst1Δ* single mutant, with volumes unchanged in *sar1-n3* and *emp24Δ* mutants (Figure 3B).

Examining the ellipsoidal nature of free vesicles, we found that WT vesicles range from ~25 to ~35 nm in their major radius, with the minor radius lying between ~15 and ~25 nm (Figure 3C), making COPII vesicles ~1.5 times longer than wide on average. Measuring the vesicle dimensions in COPII mutants using this approach revealed that the emp24Δ sec13Δ strain accumulates vesicles ~10% larger than WT cells, with the difference driven by an increase in the major axis (Figure 3C). On the other hand, we found that almost all inner coat mutants (lst1Δ, emp24Δ lst1Δ, emp24Δ) had a significantly smaller minor radius than WT vesicles, with a median of ~15 nm. Vesicles in these strains had no significant difference in major radius from WT, although the range of length in lst1Δ strains was smaller than that of WT cells (Figure 3C). The sphericity of free vesicles was calculated from the major- and minor-axis measurements, where a true sphere has sphericity of 1. WT vesicles are modestly nonspherical, with mean sphericity of 0.96 (Figure 3D); vesicles in lst1Δ, emp24Δ lst1Δ, and sar1-n3 strains showed similar sphericity (~0.95). In contrast, vesicles in emp24Δ and emp24Δ sec13Δ strains were significantly less spherical, reflected by their longer major axis than the minor axis (Figure 3, C and D).

Together, our measurements of vesicles that lack Lst1 suggest that vesicles made with Sec24 as the dominant inner coat subunit have reduced vesicle volume due to tighter curvature along one radius. Exactly what features of Lst1 and Sec24 drive these differences in membrane curvature generation remain to be tested.

Our data also suggest that the outer coat subunit, Sec13, might contribute to vesicle fission; in the absence of Sec13, vesicle length increases with no change in the minor radius, consistent with preserved membrane curvature effects, but a delay in vesicle release. The analysis of emp24Δ vesicles is intriguing; despite having all coat components, these vesicles are less spherical (i.e., flatter or more ellipsoidal) than WT vesicles. Flatter vesicles suggests that the low abundance of bulky cargo indeed facilitates membrane bending, perhaps due to low inner pressure within the vesicle lumen (Gomez-Navarro et al., 2020). Finally, our analysis shows that sar1-n3 vesicles are not morphologically different from those of WT cells, despite in vitro evidence that shows significant defects in membrane remodeling (Lee et al., 2005). One explanation for this apparent discrepancy is that ERES in the sar1-n3 mutant are more abundant on tubular ER (Figure 2D), which has significant intrinsic curvature. Tubular ER has an average radius similar to that of intermediate and late budding events (~20 nm; discussed further below; West et al., 2011), suggesting that the COPII coat can remodel tubes with less energy cost than on flat cisternae (Okamoto et al., 2012). Together, these measurements suggest that Sar1 may be involved in events other than curvature generation, which seems to be more dominantly associated with other coat components.

## Quantitative analysis of early stages of vesicle formation

Our findings suggest that the inner and outer coat play distinct roles in membrane remodeling. We next measured the ultrastructure of budding intermediates attached to the ER membrane in order to obtain quantitative information about membrane remodeling during the budding process. Buds are open contours that cannot be segmented with the approach used for free vesicles. We therefore used an alternative approach where we manually measured bud length and radius of curvature. The radius of curvature was extracted by fitting a circle to the tomographic plane with the largest bud diameter and determining the radius of that circle, whereas bud length was calculated by measuring the straight-line distance between the bud tip and the ER baseline (Figure 4A). We propose that these measurements broadly recapitulate bud progression, with

large radius of curvature and low bud length early during vesicle formation, followed by a decrease in bud radius and an increase in bud length (Figure 4B). Looking first at the global measurements of bud length and radius, we find that in WT cells, the average bud is 40 nm long with a radius of 28.5 nm (Figure 4, C and D). The emp24Δ and emp24Δ sec13Δ strains had broader distributions of bud length than WT cells, with the mean bud length significantly greater (Figure 4C). Interestingly, lst1Δ suppressed the effect of emp24Δ on bud length, with the emp24Δ lst1Δ strain resembling WT (Figure 4C). Other inner coat mutants (lst1Δ and sar1-n3 strains) also had bud lengths similar to that of WT (Figure 4C). The average bud radius was similar across all strains (Figure 4D).

By plotting bud length against radius of curvature for each individual bud, we obtained the budding profile of COPII in WT ERES (Figure 4B). Early buds are ribosome-free patches of ER with high radius of curvature and low bud length. This stage is likely followed by an increase in bud length and curvature, with buds maturing into cup-shaped structures of radius 20 to 30 nm and length ≤40 nm. The increase in curvature is followed by an increase in length by up to 80 nm, including bud neck. Knowing the average vesicle length (Figure 3), we can infer that fission takes place 50–60 nm from the bud tip. We classified each bud according to the morphology of the donor ER membrane, finding that the tubular, cisternal, or nuclear envelope origin of the membrane did not seem to correlate with a particular budding morphology (Figure 4B).

This simple yet detail-rich approach enabled us to compare the maturation of COPII buds between WT and coat mutant strains (Figure 5). Looking first at the sar1-n3 strain, we find the absence of both shallow curvature stages and very small bud lengths (Figure 5A). We note that the majority of these budding events took place at curvature-rich tubular ER (Figure 5F); bud initiation on already curved membranes with ready progression to higher curvature could explain the low frequency of shallow buds. In the emp24Δ strain, in which bulky cargo is decreased in vesicles, we see few buds with high curvature and small bud length, but more long highly curved buds than in WT (Figure 5B). Because bud length is on the average greater in this strain (Figure 4C), one interpretation is that later stages of bud formation and/or vesicle fission represent a bottleneck such that these late-stage intermediates accumulate more than in WT cells. In lst1Δ and emp24Δ lst1Δ strains, where Sec24 is the dominant inner coat subunit, membrane remodeling seems to follow a profile similar to that of WT, perhaps with a more acute transition from shallow to high curvature (Figure 5, C and D). Finally, the emp24Δ sec13Δ strain showed reduced frequency of shallow-curved buds, with most budding events apparently in mid/late stages (Figure 5E). As described earlier (Figure 2C), many of these buds were found in ERES with multiple budding sites, which suggests that membrane remodeling and curvature generation are not a limiting step in the absence of Sec13.

Our analysis of budding intermediates still attached to the donor membrane suggests that ER remodeling progresses with a relatively constant surface area (Figure 5F), such that the radius of curvature and the bud length increase simultaneously over time. Early-stage intermediates with shallow curvature (60 nm radius, 20 nm height) have a curved surface area (~7500 nm^2), which likely corresponds to a COPII-coated region, that closely matches that of buds with cup-shaped structures with no obvious bud neck (~30 nm radius, 40 nm height; surface area ~7500 nm^2). Longer buds with a characteristic omega shape have a smaller radius of curvature and a narrow bud neck (~25 nm radius and ~50 nm in length, including bud neck), yielding a surface area of ~7800 nm^2. The extra surface area of this structure likely includes uncoated regions such as the bud neck. Free vesicles
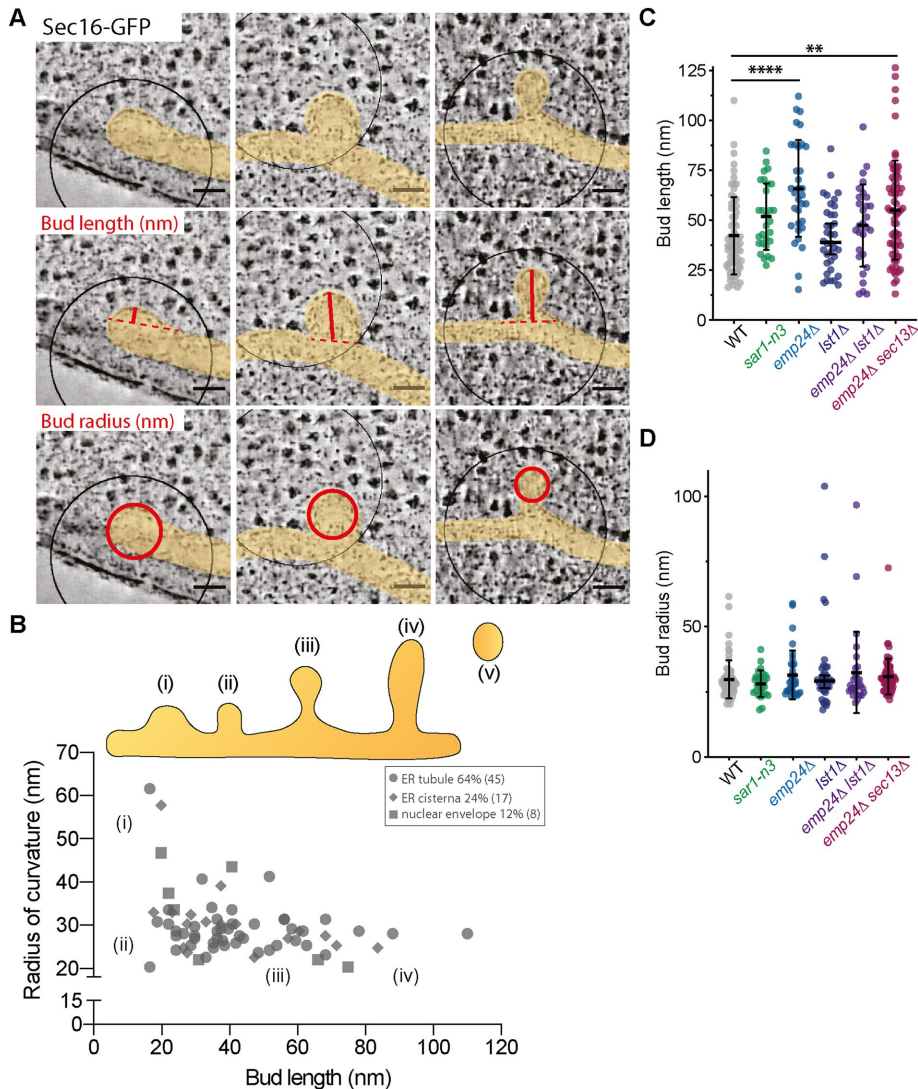
FIGURE 4: (A) Measurement of bud ultrastructure at WT ERES (black circle represents a 250-nm circle around the centroid of the Sec16-GFP spot; ER membranes false colored in yellow). Bud length and bud radius were calculated from tomograms of various budding morphologies including shallow buds (left panels), cup-shaped structures (middle panels), and omega-shaped structures/tubes (right panels). Bud length corresponds to the distance between the tip of the bud to the ER baseline (solid red lines), whereas bud radius was determined by fitting a circle at the equatorial plane of the budding event (solid red circles). (B) Distribution of WT budding events as a function of bud length and radius. Bud maturation steps can be categorized as (i) shallow buds of small curvature and short length, (ii) early buds of large curvature and short length, (iii) late buds with large curvature and elongated bud neck, and (iv) very long buds with large curvature. Each point represents a single budding event in a WT strain with the ER morphology at the bud site indicated by the shape of the datapoint, as depicted in the inset and with the indicated frequency. Circle = ER tubule, diamond = ER cisterna, and square = nuclear envelope. (C) Plot of bud lengths (nm) of individual buds in the indicated strains. Bars represent the median with 95% confidence interval. (D) Plot of bud radius (nm) of individual buds in the indicated strains. Number of buds measured per strain: WT $n = 70$, sar1n3 $n = 28$, emp24 $n = 33$, lst1Δ $n = 36$, emp24Δ lst1Δ $n = 29$, emp24Δ sec13Δ $n = 70$. Bars represent the median with 95% confidence interval. Statistical test was a one-way ANOVA with Tukey's correction for multiple comparisons where all five mutant strains were compared with WT (* $p < 0.05$; ** $p < 0.01$; *** $p < 0.001$; **** $p < 0.0001$).

have an average surface of ~5700 nm² (Gomez-Navarro et al., 2020), suggesting some loss of membrane surface area is associated with vesicle fission and release. Electron cryotomography will be required to visualize coats directly on these curved membranes.
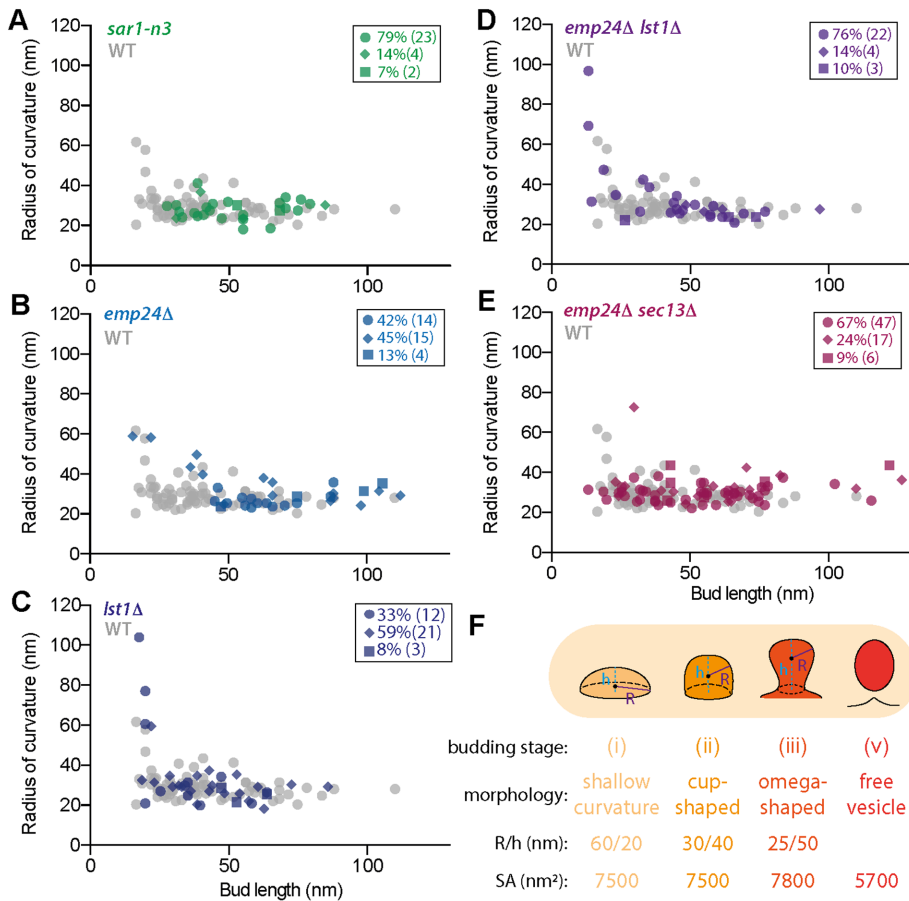
DISCUSSION

CLEM is a powerful tool for investigating the ultrastructure of membranes within cells. Here, we have measured various properties of vesicles and budding intermediates at ERES in yeast. Genetic modification of coat components or cargo abundance significantly modifies the behavior of the coat and subsequently the ultrastructure of buds and vesicles. By systematically analyzing membrane features in various COPII mutants, we have obtained new insight into the contributions of different components.

A key finding of our CLEM analysis of coat mutants is that the inner coat likely plays a significant role in membrane remodeling. Pioneering in vitro reconstitutions and structural studies have long suggested that the mechanical force to bend the ER membrane comes predominantly from the rigid cage of Sec13/Sec31 (Barlowe et al., 1994; Bacia et al., 2011). More recent structural evidence, however, indicates that assembly of the inner coat (Sar1-Sec23/Sec24) might also drive membrane remodeling, so that organization into helical arrays is associated with tubulation of large synthetic liposomes (Zanetti et al., 2013; Hutchings et al., 2021). Consistent with a significant role for the inner coat in curvature generation, our tomography revealed that lack of Sec13, which likely results in a less rigid Sec31 cage, does not prevent the formation of buds and vesicles with high curvature. The caveat to this conclusion is that loss of bulky cargo (i.e., emp24Δ) is required for this permissive membrane-bending condition.

If a rigid Sec13/31 cage is not absolutely necessary to achieve high curvature, what is the role of the outer coat in membrane remodeling and why does Sec31 stiffness matter? Our analysis of bud and vesicle length might shed light on this. Although both emp24Δ and emp24Δ sec13Δ mutants have long buds, only in the emp24Δ sec13Δ does this result in elongated vesicles. Long vesicles could arise from alternative organization of Sec31 in the absence of Sec13; however, longer vesicles could also be a consequence of delays in bud fission. Consistent with this, a majority of emp24Δ sec13Δ ERES are multibudded structures, and we have previously observed "beads-on-a-string" bud morphology in this strain background (Gomez-Navarro et al., 2020). Together, these morphologies are consistent with delayed vesicle release from the donor membrane, resulting in higher steady state abundance of mature buds. We propose that membrane remodeling toward shallow curvature is driven by inner coat assembly; a rigid Sec13/Sec31 scaffold then encapsulates the membrane to form a structure with an elongated bud neck, which would facilitate

FIGURE 5: (A–E), Bud morphology as described for Figure 4B comparing WT (gray datapoints) and indicated strains (colored datapoints) showing the distribution of budding events as a function of bud length (nm) and radius of curvature (nm). Inset panels indicate the bud origin, where circle = ER tubule, diamond = ER cisterna, and square = nuclear envelope. (F) Bar plot indicating the frequency (%) of buds per ER subregion in WT and dysfunctional COPII strains. Number of buds measured per strain: WT *n* = 70, *sar1-n3* *n* = 28, *emp24* n = 33, *lst1Δ* n = 36, *emp24Δ lst1Δ* n = 29, *emp24Δ sec13Δ* n = 70.

Once bud site selection has occurred, local recruitment of the inner coat would initiate membrane bending, driven by lateral assembly of Sar1-Sec23-Sec24 units (Figure 6A). As the bud reaches high curvature, the steric pressure associated with locally enriched adaptor-bound cargo crowding increases the energetic cost of changing membrane curvature (Derganc *et al.*, 2013; Figure 6B). Sar1 may locally reduce the bending modulus of the lipid bilayer and facilitate spontaneous positive curvature (Hanna *et al.*, 2016; Lee *et al.*, 2005; Loftus *et al.*, 2012; Settles *et al.*, 2010), thus counterbalancing the growing repulsive forces within the ER lumen as the coat polymerizes (Copic *et al.*, 2012). Moreover, the lipid environment may be locally remodeled with lipid species that facilitate membrane bending or stabilize cargo under the unfavorable conditions of the vesicle lumen (Melero *et al.*, 2018; Jiménez-Rojo *et al.*, 2019; Rodriguez-Gallardo *et al.*, 2020). Recruitment of Sec13/Sec31 rods would promote the ordered arrangement of the inner coat (Ma and Goldberg, 2016; Hutchings *et al.*, 2021), thus reducing the bud radius (Gomez-Navarro *et al.*, 2020). Polymerization of Sec13/Sec31 into a rigid cage around the bud tip would further increase the pressure within the bud, which may translate into a local increase in surface tension and the appearance of a bud neck (Raote *et al.*, 2020). The bud neck is probably free of coat and cargo, but will be mechanically stressed, facilitating spontaneous fission of the membrane and release of a free vesicle (Figure 6). This model explains our observations of high frequency of vesicles in *lst1Δ* and *sar1-n3*

spontaneous or Sar1-mediated fission (Figure 6). A less rigid cage would lack the necessary structural stiffness to counteract pressure within the bud, thereby generating larger buds without a narrow bud neck where fission could occur.

The capacity of the coat to sense and modify the physical properties of the membrane seems to be critical to both initiate a budding site and determine vesicle ultrastructure. Neither bending rigidity nor membrane tension is uniform, either throughout the cell or over the remodeling process. Thus, the coat likely needs diverse strategies to impose the required shape changes needed to ultimately drive fission. Low membrane-bending rigidity and high spontaneous curvature are desirable features to initiate budding. ER ultrastructure is actively remodeled via shape changes and insertion of new lipids, both of which may favor the spontaneous appearance of conditions suitable for budding. Sar1 might sense such favorable conditions (intrinsic curvature and low bending rigidity; Doucet *et al.*, 2015) and together with Sec16 drive COPII recruitment to suitable regions of the ER. In yeast, the ER membrane is studded with numerous ribosomes, which need to be cleared to permit coat assembly and membrane remodeling. How ribosome clearance is coordinated with COPII recruitment remains unclear, but the large size and intrinsic disorder of Sec16 suggest that one of its roles may be to prepare an appropriately cleared region of ER membrane.

strains, where small bud radius (*lst1Δ*) and limited capacity to reduce rigidity (*sar1-n3*) may promote early membrane fission and vesicle release. Our model is also in agreement with previous in vitro observations, where COPII has been found to favor polymerization on liposomes with low membrane bending rigidity (Melero *et al.*, 2018), similarly to other coat complexes (Manneville *et al.*, 2008; Saleem *et al.*, 2015; Mercier *et al.*, 2020).

Given the conserved structures of COPII coat subunits across species, our observations in yeast are likely relevant to other organisms, despite clear differences in the morphology of ERES. In animal cells, secretion of very large cargo such as procollagen fibers is difficult to reconcile with classic COPII secretion models (McCaughey *et al.*, 2018). A recent theoretical study suggests that modulating bud tension could prevent fission and lead to the formation of pearled buds, which would support export of procollagen fibers (Raote *et al.*, 2020). Our data support the preferred formation of pearled buds if the physical stiffness of the Sec13/Sec31 cage is reduced (Figure 2C, Supplemental Figure S2, and Gomez-Navarro *et al.*, 2020), thus supporting the possibility of such an export mechanism for large cargo in animal cells. Recent studies have described large tubular and multibudded ERES in human cells, where COPI machinery may also be required for ER-to-Golgi trafficking (Shomron *et al.*, 2021; Weigel *et al.*, 2021). Weigel and colleagues found that

a sudden accumulation of cargo increases the volume of ERES, which may hinder the capacity of the coat to induce membrane fission, similarly to the situation we observe in *emp24Δ sec13Δ* cells. Further application of CLEM approaches, including cryo-electron tomography to visualize coat organization in situ, will help illuminate whether the principles of coat assembly and membrane remodeling we propose here are conserved in human cells.

MATERIALS AND METHODS

Request a protocol through *Bio-protocol*.

Strains and plasmids

All strains were generated and maintained using standard *S. cerevisiae* methods. Strains were made by PCR-based integration of sfGFP fused in-frame at the 3′ end of the *SEC16* locus using drug-resistance markers. Strain *emp24Δ sec13Δ SEC16-sfGFP pSEC13-URA3* was plated onto media containing 5-FOA to counter select for the *SEC13-URA3* plasmid.

List of strains:

LMY1277: MATa SEC16-sfGFP:kanMX his3Δ1 leu2Δ0 met15Δ0 ura3Δ0

LMY1281: MATa sar1Δ::kanMX Sar1n3::LEU2 SEC16sfGFP:TRP ura3 lys2 ade2 trp1 his3 leu2.

MAY030: MATa emp24Δ::kanMX SEC16sfGFP:HIS3 his3Δ1 leu2Δ0 met15Δ0 ura3Δ0

LMY1280: MATa lst1Δ::kanMX SEC16sfGFP:HIS3 his3Δ1 leu2Δ0 met15Δ0 ura3Δ0

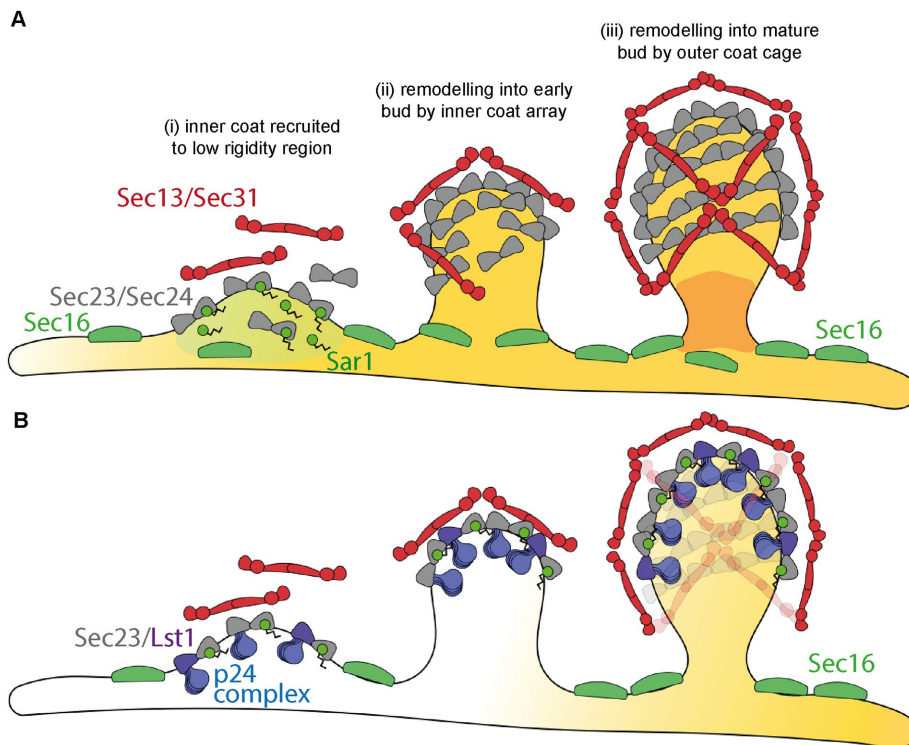LMY1279: MATa emp24Δ::kanMX lst1Δ::natMX SEC16sfGFP:HIS3 his3Δ1 leu2Δ0 met15Δ0 ura3Δ0.

LMY1278: MATa emp24Δ::natMX sec13Δ::HIS3 pLM246(CEN::SEC13-URA3) SEC16sfGFP:kanMX his3Δ1 leu2Δ0 met15Δ0 ura3Δ0

GFP imaging

For imaging of Sec16-sfGFP, cells were grown at 25°C in minimal media lacking tryptophan. Images were taken on a Nikon Ti2 with a 100×/1.49 NA Oil (TIRF) objective and a Hamamatsu ORCA-FLASH 4.0 C11330-22C camera using a scientific complementary metal oxide-semiconductor (sCMOS) sensor. The same imaging methodology was used for the imaging of EM grids with sections of resin-embedded cells.

Endoplasmic reticulum exit site analysis

z-stacks using 0.2-μm *z* spacing of epifluorescence images were acquired as described above. Cells were manually selected with the elliptical selection tool in FIJI and assigned as a region of interest. ERES were then localized with a difference of Gaussian (DoG) using a custom FIJI script. The local maxima of the DoG and a threshold based on a false alarm rate were combined to localize bright local maxima. Localized spots were then rendered as Gaussian spots and added as a second channel for visual validation. The macro is available on GitHub: https://github.com/jboulanger/imagej-macro/tree/main/Detect_Spots. Statistical analysis was performed with Prism 7.0 (GraphPad Software).

Correlative light and electron microscopy

CLEM was performed as described in Kukulski *et al.* (2011) with some modifications as described in Ader and Kukulski (2017). Yeast cells were grown at 25°C in minimal media lacking tryptophan to 0.6–0.8 OD600d, pelleted by vacuum filtration onto nitrocellulose discs, and then placed on an agar plate to prevent the pellets from drying out. The yeast paste was high-pressure frozen in 200 μm–deep wells of aluminum carriers (Wohlwend) using a HPM100 (Leica Microsystems). Freeze substitution and Lowicryl HM20 (Polysciences) resin embedding were done as previously described in Kukulski *et al.* (2011), with minor modifications. Uranyl acetate in acetone (0.03%) was used for freeze substitution. Samples were shaken on dry ice for the first 2–3 h of freeze substitution (McDonald and Webb, 2011). Sections 300 nm thick were cut with an Ultra 45° diamond knife (Diatome) on an Ultracut E microtome (Reichert). The sections were floated onto PBS and picked up with 200 mesh carbon-coated copper grids (AGS160, Agar Scientific). Fluorescent TetraSpeck beads (Invitrogen), 50 nm in diameter, were adsorbed onto the grid. Immediately after sectioning, grids were mounted for fluorescence microscopy (described above). Before electron tomography, 15-nm gold beads (Electron Microscopy Sciences) were adsorbed onto

A

(i) inner coat recruited to low rigidity region

Sec13/Sec31

Sec23/Sec24

Sec16

Sar1

(ii) remodelling into early bud by inner coat array

(iii) remodelling into mature bud by outer coat cage

Sec16

B

Sec23/Lst1

p24 complex

Sec16

FIGURE 6: (A) Schematic representing the stages of vesicle formation, starting with coat assembly at low-rigidity regions of the ER facilitated by Sar1 (i), triggering initial membrane remodeling into an early bud driven by the lateral assembly of arrays of inner coat subunits (ii). As the bud progresses, the outer coat assembles into a polyhedral structure (iii), which on one hand constrains the radius of the bud and on the other organizes the inner coat into a denser array. Outer coat assembly promotes the growth of the bud in length, increasing tension at the bud neck and facilitating its spontaneous fission. (B) A schematic view of the lumen of the maturing bud depicting the increase lateral pressure of the cargo bound to the inner coat.

the sections, which were then poststained for 15 min with lead citrate. Scanning transmission EM tomography was done on a TF20 microscope (FEI) with an axial brightfield detector, using a camera length of 200 mm and a 50-mm C2 aperture (Ader and Kukulski, 2017; Hohmann-Marriott et al., 2009). For correlation to fluorescence images, low-magnification tilt series at pixel size 3.1 nm were acquired using SerialEM (±55° tilt range, 2° increment, single axis acquisition; Mastronarde, 2005). Higher magnification tomograms were acquired as dual-axis tilt series ±60° with 1° increment and at pixel size 1.1 nm (Mastronarde, 1997). All tomographic reconstructions were done in IMOD (Kremer et al., 1996), and fiducial-based correlation was done using MATLAB- based scripts described in Kukulski et al. (2011) except for supplemental Figure S2 overlay (right panel), which was done using Icy EC-CLEM (Paul-Gilloteaux et al., 2017).

After correlation of the Sec16-sfGFP signal, a circular area of radius 125 nm was placed on the centroid of the correlation. Buds and vesicles within this circular area were considered as part of an ERES. Frequency of free vesicles in the correlated region was calculated as the total number of vesicles divided by the total number of correlated sites. For ER morphology determination, we first identified the ER as a membranous organelle with numerous electron-dense ribosomes attached, frequently found in close proximity to PM and mitochondria. ER was considered cisternal when two parallel ER membranes were observed across the z axis, fusing at a cisterna edge only once. Tubular shape was designated when non–nuclear envelope membranes were not cisternal, generally corresponding to a hollow quasi-cylindrical structure of various diameters following irregular shapes across the z axis of the tomogram. Golgi complex structures were identified as flat fenestrated parallel membranes (≤45 nm wide) with round budlike extremes. Golgi complex cisterna also presented an exclusion zone for ribosomes.

Segmentation analysis

Free vesicles (Figure 3) were manually segmented using IMOD. Vesicles axis and volume quantifications were obtained with FIJI using the plugin LimeSeg (Machado et al., 2019) as follows: the outer contour of a vesicle was selected as the region of interest (ROI) using the "point tool" and "segmented line" tool moving in z through the tomographic slices. The lowest plane of the vesicle was annotated as a ROI with the point tool; then contours were selected with the segmented line tool every five virtual slices before finally closing the volume with the top plane of the vesicle using the point tool. LimeSeg Skeleton Segmentation tool settings were adjusted to recognize and segment the outer surface of the vesicle (D_0: 4, F_pressure: 0, Z_scale: 1, Range_in_DO_units: 1, NumberOfIntegrationStep: −1, RealXYPixelSize: 1). After the segmentation was run, the correct distribution of surfels over the outer contour of the vesicle was assessed by eye. The LimeSeg segmentation tool provides the list of vertices of the mesh. The centroid of this point cloud gives an estimate the center of the segmented vesicle. The maximum radius was then computed as the maximum distance to this center considering the $1.1 \times 1.1 \times 1.1$–nm voxel size. Sphericity was determined according to the formula $(\pi^{1/3} \times (6V)^{2/3})/A$. Statistical analysis was performed with Prism 7.0 (GraphPad Software).

Bud surface area estimation

The surface area of early and medium buds was calculated using the formula $SA = 2\pi Rh$, where R is the bud radius and h is the bud length. The surface area of late buds was calculated assuming a nearly spherical ellipsoid, using the expression $SA \approx 4\pi^{1.6} \dfrac{\sqrt{a^{1.6}b^{1.6} + a^{1.6}c^{1.6} + b^{1.6}c^{1.6}}}{3}$. All calculations were made using https://www.calculator.net/surface-area-calculator.html.

REFERENCES

Ader NR, Kukulski W (2017). Chapter 14 - triCLEM: Combining high-precision, room temperature CLEM with cryo-fluorescence microscopy to identify very rare events. In: Correlative Light and Electron Microscopy III, ed. T. Müller-Reichert and P. Verkade, Academic Press, Vol. 140, 303–320.

Antonny B, Madden D, Hamamoto S, Orci L, Schekman R (2001). Dynamics of the COPII coat with GTP and stable analogues. Nat Cell Biol 3, 531–537.

Bacia K, Futai E, Prinz S, Meister A, Daum S, Glatte D, Briggs JAG, Schekman R (2011). Multibudded tubules formed by COPII on artificial liposomes. Sci Rep 1, 17.

Barlowe C, Orci L, Yeung T, Hosobuchi M, Hamamoto S, Salama N, Rexach MF, Ravazzola M, Amherdt M, Schekman R (1994). COPII: a membrane coat formed by Sec proteins that drive vesicle budding from the endoplasmic reticulum. Cell 77, 895–907.

Bi X, Mancias JD, Goldberg J (2007). Insights into COPII coat nucleation from the structure of Sec23•Sar1 complexed with the active fragment of Sec31. Dev Cell 13, 635–645.

Bonifacino JS, Glick BS (2004). The mechanisms of vesicle budding and fusion. Cell 116, 153–166.

Copic A, Latham CF, Horlbeck MA, D'Arcangelo JG, Miller EA (2012). ER cargo properties specify a requirement for COPII coat rigidity mediated by Sec13p. Science (New York, NY) 335, 1359–1362.

D'Arcangelo JG, Crissman J, Pagant S, Čopič A, Latham CF, Snapp EL, Miller EA (2015). Traffic of p24 proteins and COPII coat composition mutually influence membrane scaffolding. Curr Biol 25, 1296–1305.

Derganc J, Antonny B, Copič A (2013). Membrane bending: the power of protein imbalance. Trends Biochem Sci 13, 1–9.

Doucet CM, Esmery N, de Saint-Jean M, Antonny B (2015). Membrane curvature sensing by amphipathic helices is modulated by the surrounding protein backbone. PLoS One 10, e0137965.

Faini M, Beck R, Wieland FT, Briggs JAG (2013). Vesicle coats: structure, function, and general principles of assembly. Trends Cell Biol 23, 279–288.

Ghaemmaghami S, Huh WK, Bower K, Howson RW, Belle A, Dephoure N, O'Shea EK, Weissman JS (2003). Global analysis of protein expression in yeast. Nature 425, 737–741.

Gomez-Navarro N, Melero A, Li XH, Boulanger J, Kukulski W, Miller EA (2020). Cargo crowding contributes to sorting stringency in COPII vesicles. J Cell Biol 219, e201806038.

Hanna MG, Mela I, Wang L, Henderson RM, Chapman ER, Edwardson JM, Audhya A (2016). Sar1 GTPase activity is regulated by membrane curvature. J Biol Chem 291, 1014–1027.

Hohmann-Marriott MF, Sousa AA, Azari AA, Glushakova S, Zhang G, Zimmerberg J, Leapman RD (2009). Nanoscale 3D cellular imaging by axial scanning transmission electron tomography. Nat Methods 6, 729–731.

Hutchings J, Stancheva VG, Brown NR, Cheung ACM, Miller EA, Zanetti G (2021). Structure of the complete, membrane-assembled COPII coat reveals a complex interaction network. Nat Commun 12, 2034.

Hutchings J, Stancheva V, Miller EA, Zanetti G (2018). Subtomogram averaging of COPII assemblies reveals how coat organization dictates membrane shape. Nat Commun 9, 4154.

Jiménez-Rojo N, Leonetti M, Zoni V, Colom A, Feng S, Iyengar N, Matile S, Roux A, Vanni S, Weissman J, et al. (2019). Conserved function of ether lipids and sphingolipids in the early secretory pathway. Curr Biol 1–13.

Kremer JR, Mastronarde DN, McIntosh JR (1996). Computer visualization of three-dimensional image data using IMOD. J Struct Biol 116, 71–76.

Kukulski W, Schorb M, Welsch S, Picco A, Kaksonen M, Briggs JAG (2011). Correlated fluorescence and 3D electron microscopy with high sensitivity and spatial precision. J Cell Biol 192, 111–119.

Kung LF, Pagant S, Futai E, D'Arcangelo JG, Buchanan R, Dittmar JC, Reid RJD, Rothstein R, Hamamoto S, Snapp EL, *et al.* (2011). Sec24p and Sec16p cooperate to regulate the GTP cycle of the COPII coat. EMBO J 31, 1014–1027.

Kurokawa K, Suda Y, Nakano A (2016). Sar1 localizes at the rims of COPII-coated membranes in vivo. J Cell Sci 129, 3231–3237.

Lee MCS, Orci L, Hamamoto S, Futai E, Ravazzola M, Schekman R (2005). Sar1p N-terminal helix initiates membrane curvature and completes the fission of a COPII vesicle. Cell 122, 605–617.

Loftus AF, Hsieh VL, Parthasarathy R (2012). Modulation of membrane rigidity by the human vesicle trafficking proteins Sar1A and Sar1B. Biochem Biophys Res Commun, 426, 585–589.

Ma W, Goldberg J (2016). TANGO1/cTAGE5 receptor as a polyvalent template for assembly of large COPII coats. Proc Natl Acad Sci 113, 10061–10066.

Machado S, Mercier V, Chiaruttini N (2019). LimeSeg: A coarsed-grained lipid membrane simulation for 3D image segmentation. BMC Bioinformatics 20, 2.

Malhotra V, Erlmann P, Nogueira C (2015). Procollagen export from the endoplasmic reticulum. Biochem Soc Trans 43, 104–107.

Manneville J-B, Casella J-F, Ambroggio E, Gounon P, Bertherat J, Bassereau P, Cartaud J, Antonny B, Goud B (2008). COPI coat assembly occurs on liquid-disordered domains and the associated membrane deformations are limited by membrane tension. Proc Natl Acad Sci 105, 16946–16951.

Manzano-Lopez J, Perez-Linero AM, Aguilera-Romero A, Martin ME, Okano T, Silva DV, Seeberger PH, Riezman H, Funato K, Goder V, *et al.* (2015). COPII coat composition is actively regulated by luminal cargo maturation. Curr Biol 25, 152–162.

Mastronarde DN (2005). Automated electron microscope tomography using robust prediction of specimen movements. J Struct Biol 152, 36–51.

Mastronarde DN (1997). Dual-axis tomography: An approach with alignment methods that preserve resolution. J Struct Biol 120, 343–352.

McCaughey J, Stevenson NL, Cross S, Stephens DJ (2018). ER-to-Golgi trafficking of procollagen in the absence of large carriers. J Cell Biol 218, 929–948.

McDonald KL, Webb RI (2011). Freeze substitution in 3 hours or less. J Microsc 243, 227–233.

Melero A, Chiaruttini N, Karashima T, Riezman I, Funato K, Barlowe C, Riezman H, Roux A (2018). Lysophospholipids facilitate COPII vesicle formation. Curr Biol 28, 1950–1958.

Mercier V, Larios J, Molinard G, Goujon A, Matile S, Gruenberg J, Roux A (2020). Endosomal membrane tension regulates ESCRT-III-dependent intra-lumenal vesicle formation. Nat Cell Biol 22, 947–959.

Miller E, Antonny B, Hamamoto S, Schekman R (2002). Cargo selection into COPII vesicles is driven by the Sec24p subunit. EMBO J 21, 6105–6113.

Miller EA, Barlowe C (2010). Regulation of coat assembly—sorting things out at the ER. Curr Opin Cell Biol 22, 447–453.

Okamoto M, Kurokawa K, Matsuura-Tokita K, Saito C, Hirata R, Nakano A (2012). High-curvature domains of the ER are important for the organization of ER exit sites in *Saccharomycescerevisiae*. J Cell Sci 125, 3412–3420.

Paul-Gilloteaux P, Heiligenstein X, Belle M, Domart MC, Larijani B, Collinson L, Raposo G, Salamero J (2017). EC-CLEM: Flexible multidimensional registration software for correlative microscopies. Nat Methods 14, 102–103.

Raote I, Ortega-Bellido M, Santos AJM, Foresti O, Zhang C, Garcia-Parajo MF, Campelo F, Malhotra V (2018). TANGO1 builds a machine for collagen export by recruiting and spatially organizing COPII, tethers and membranes. eLife 7, e32723.

Raote I, Chabanon M, Walani N, Arroyo M, Garcia-Parajo MF, Malhotra V, Campelo F (2020). A physical mechanism of tango1-mediated bulky cargo export. eLife 9, e59426.

Rodriguez-Gallardo S, Kurokawa K, Sabido-Bozo S, Cortes-Gomez A, Ikeda A, Zoni V, Aguilera-Romero A, Perez-Linero AM, Lopez S, Waga M, *et al.* (2020). Ceramide chain length–dependent protein sorting into selective endoplasmic reticulum exit sites. Sci Adv 6, 1–12.

Saleem M, Morlot S, Hohendahl A, Manzi J, Lenz M (2015). A balance between membrane elasticity and polymerization energy sets the shape of spherical clathrin coats. Nat Commun 6, 6249.

Settles EI, Loftus AF, McKeown AN, Parthasarathy R (2010). The vesicle trafficking protein Sar1 lowers lipid membrane rigidity. Biophys J 99, 1539–1545.

Shimoni Y, Kurihara T, Ravazzola M, Amherdt M, Orci L, Schekman R (2000). Lst1p and Sec24p cooperate in sorting of the plasma membrane ATPase into COPII vesicles in *Saccharomycescerevisiae*. J Cell Biol 151, 973–984.

Shomron O, Nevo-yassaf I, Aviad T, Yaffe Y, Zahavi EE, Dukhovny A, Perlson E, Brodsky I (2021). COPII collar defines the boundary between ER and ER exit site and does not coat cargo containers. J Cell Biol 220, e201907224.

Stachowiak JC, Brodsky FM, Miller EA (2013). A cost–benefit analysis of the physical mechanisms of membrane curvature. Nat Cell Biol 15, 1019–1027.

Stagg SM, Gürkan C, Fowler DM, LaPointe P, Foss TR, Potter CS, Carragher B, Balch WE (2006). Structure of the Sec13/31 COPII coat cage. Nature 439, 234–238.

Stancheva VG, Li XH, Hutchings J, Gomez-Navarro N, Santhanam B, Madan Babu M, Zanetti G, Miller EA (2020). Combinatorial multivalent interactions drive cooperative assembly of the COPII coat. J Cell Biol 219, e202007.

Weigel AV, Chang C, Shtengel G, Qiu W, Hess HF, Lippincott-Schwartz J (2021). ER-to-Golgi protein delivery through an interwoven, tubular network extending from ER. Cell 184, 2412–2429.

West M, Zurek N, Hoenger A, Voeltz GK (2011). A 3D analysis of yeast ER structure reveals how ER domains are organized by membrane curvature. J Cell Biol 193, 333–346.

Zanetti G, Prinz S, Daum S, Meister A, Schekman R, Bacia K, Briggs JA (2013). The structure of the COPII transport-vesicle coat assembled on membranes. ELife 2, e00951.